Journal of Materials Chemistry A

ROYAL SOCIETY OF CHEMISTRY

PAPER

View Article Online
View Journal

Published on 04 May 2020. Downloaded by University of South Carolina Libraries on 5/18/2020 1:19:33 PM.

Check for updates

Cite this: DOI: 10.1039/d0ta03476b

Structural evolution, electrochemical kinetic properties, and stability of A-site doped perovskite $Sr_{1-x}Yb_xCoO_{3-\delta}$†

Chunyang Yang,[a] Yun Gan,[a] Myongjin Lee,[a] Chunlei Ren,[a] Kyle S. Brinkman,[b] Robert D. Green[c] and Xingjian Xue *[a]

Mixed ionic and electronic conducting (MIEC) perovskite $SrCoO_{3-\delta}$ is a widely studied (electro)catalyst for the oxygen reduction reaction (ORR) and possesses different crystal structures at different temperatures. These temperature dependent phase transitions significantly impact the ordering of oxygen vacancies and electrochemical kinetic properties as well as the reliability of the related devices. Some of the crystal structures formed, *e.g.* hexagonal phases, turn out to be almost impermeable to oxygen gas. Therefore, it is important to stabilize the crystal structure of $SrCoO_{3-\delta}$ that favors the ORR over a wide temperature range. Herein, the partial substitution of the A-site Sr with Yb is systematically studied, including synthesis, characterization and analysis of structural evolution, electrochemical kinetic properties, thermal stability, and stability in a CO_2-containing atmosphere. The results indicate that $Sr_{0.90}Yb_{0.10}CoO_{3-\delta}$ is able to stabilize the tetragonal crystal structure with less ordered oxygen vacancies, leading to polarization resistances of 0.051, 0.115 and 0.272 Ω cm^2 at 750, 700 and 650 °C, respectively, on symmetrical cells. $Sr_{0.90}Yb_{0.10}CoO_{3-\delta}$ demonstrates a very stable surface oxygen vacancy distribution and electronic structure near oxygen vacancies but dissociation of adsorbed oxygen molecules into atomic oxygen is affected by surface Sr segregation, and polarization resistance degradation is mainly induced by surface Sr segregation. Furthermore, $Sr_{0.90}Yb_{0.10}CoO_{3-\delta}$ exhibits excellent thermal stability as well as excellent recovery stability and improved polarization performance after a few pure air/CO_2-containing air treatment cycles at 700 °C. However, a hysteresis behavior of polarization performance is observed at 650 °C during gas cycling treatment, which may cause long-term degradation of the $Sr_{0.90}Yb_{0.10}CoO_{3-\delta}$ electrode. The different polarization behaviors during gas cycling treatment are induced by different sensitivities of the formed surface strontium carbonate and chemisorbed surface oxo-carbonaceous species to different operating temperatures.

Received 28th March 2020
Accepted 4th May 2020

DOI: 10.1039/d0ta03476b

rsc.li/materials-a

1. Introduction

Solid oxide fuel cells (SOFCs) convert chemical energy in fuels into electrical energy in a highly efficient and environmentally friendly manner, and have been widely studied.[1] In order to obtain high electrochemical performance, early stage SOFCs are usually operated at high temperatures (above 800 °C). This operating temperature may increase system and operating cost, limit material selections, and cause material and microstructure degradation.[2] To overcome these issues, it is suggested that the operating temperature of SOFCs be reduced to an intermediate range (600–800 °C).[1,3] Nevertheless, lowering the operating temperature would increase the resistance losses of charge transport and surface exchange kinetic processes, especially polarization losses induced by the cathodic electrode process.[4] Thus, it is very important to develop cathode materials suitable for intermediate temperature SOFCs (IT-SOFCs).

Perovskite-type mixed ionic and electronic conducting (MIEC) materials have high flexibility to tune their physical properties such as oxygen vacancies, structural symmetry, lattice free volumes, and metal–oxygen bonding energies. These properties are strongly dependent on the crystal structure and significantly affect the electrochemical kinetic properties and stability of the materials.[5,6] Strontium cobaltite ($SrCoO_{3-\delta}$) is a typical MIEC perovskite showing high electrical conductivity and electrocatalytic properties as a cathode material for SOFCs and has been widely used as a parent compound to derive other high performance MIEC cathodes.[7] Depending on the annealing temperature and oxygen partial pressure during the synthesis/fabrication process, $SrCoO_{3-\delta}$ may adopt a variety of crystal structures, *e.g.* orthorhombic, tetragonal and cubic. For

[a]Department of Mechanical Engineering, University of South Carolina, Columbia, SC 29208, USA. E-mail: Xue@cec.sc.edu; Fax: +1-803-777-0106; Tel: +1-803-576-5598
[b]Materials Science and Engineering, Clemson University, Clemson, SC 29634, USA
[c]NASA Glenn Research Center, Cleveland, OH 44135, USA

† Electronic supplementary information (ESI) available. See DOI: 10.1039/d0ta03476b

Published on 04 May 2020. Downloaded by University of South Carolina Libraries on 5/18/2020 1:19:33 PM.

example, $SrCoO_{3-\delta}$ forms an oxygen vacancy-ordered orthorhombic brownmillerite phase below 653 °C, and will transfer to a 2-H type hexagonal phase between 653 and 920 °C, eventually changing to a cubic or tetragonal perovskite phase above 920 °C. However, the high temperature phase will transit reversibly to a hexagonal phase as temperature drops from a high (>920 °C) to an intermediate temperature range.[8] These phase variations directly affect the oxygen vacancy features and the electrochemical properties of $SrCoO_{3-\delta}$. For example, the vacancy ordered state at low temperatures transforms to a disordered state above 900 °C; the resulting hexagonal phase is almost impermeable to oxygen gas.[9] Interestingly, the high temperature phase of $SrCoO_{3-\delta}$, a cubic phase, demonstrates the best electrochemical kinetic properties among all the phases.[7,10] Therefore, it is important to stabilize the cubic phase of $SrCoO_{3-\delta}$ in a wide temperature range (from high to room temperature) to prevent phase transition reversibly upon temperature decrease.

The Goldschmidt tolerance factor is able to describe the distortion degree of a perovskite structure from the standard cubic one. To form a cubic perovskite structure, the corresponding Goldschmidt tolerance factor should be close to 1. Given the ionic radius of $r(Sr^{2+})$(XII) = 1.44 Å, $r(Co^{4+})$(VI) = 0.53 Å, and $r(O^{2-})$(VI) = 1.40 Å,[11] the theoretical Goldschmidt tolerance factor of an ideal stoichiometric perovskite, $SrCoO_3$, is 1.04. To tune the tolerance factor closer to 1, two doping strategies can be utilized. One is B-site doping using elements with ionic radii greater than $r(Co^{4+})$(VI), such as Nb, Sc, Ti, Sb, Mo and Ta.[12–18] However, a relatively high content of such elements, *e.g.* up to 20 mol% B-site doping, is required in order to stabilize the cubic phase. This could deteriorate the oxygen reduction reaction properties of the material, which are strongly dependent on the valence and spin state of the B-site elements. Another strategy is to dope an element with a smaller size than $r(Sr^{2+})$(XII) on the A-site, which is much less studied in the literature. The radii of lanthanides in 12-fold coordinates decrease with an increase in atomic number, *e.g.* $r(La^{3+})$(XII) = 1.36 Å, $r(Ce^{3+})$(XII) = 1.34 Å, $r(Nd^{3+})$(XII) = 1.27 Å and $r(Sm^{3+})$(XII) = 1.24 Å. Even though the exact radius of Yb^{3+}(XII) is not available in the radius chart, it is anticipated that the radius of Yb^{3+} in 12-fold coordinates would be smaller than that of Sm^{3+}.[11] This is consistent with those reported in other references, *i.e.*, 1.22 Å,[19] 1.07 Å [20] and 1.01 Å [21] for Yb^{3+} in 12-fold coordinates. Therefore, a partial substitution of Sr by Yb on the A-site is expected to be able to tune the tolerance factor closer to 1, potentially stabilizing the cubic perovskite structure of $SrCoO_{3-\delta}$.

It has been recognized that Sr in $SrCoO_{3-\delta}$ can be demixed and segregated onto the surface of a bulk cathode, leading to deterioration of electrode performance.[22,23] Under practical operating conditions, an oxygen/air atmosphere surrounding the SOFC cathode could contain a small amount of CO_2. When exposed to a CO_2-containing atmosphere, surface Sr could react with CO_2 to form carbonates on the oxide surface, blocking oxygen surface exchange.[24,25] For instance, the polarization resistances of $Ba_{0.5}Sr_{0.5}Co_{0.8}Fe_{0.2}O_{3-\delta}$ and $SrSc_{0.175}Nb_{0.025}Co_{0.8}O_{3-\delta}$ cathodes increase about 25 and 35 times, respectively, when exposed to 5% CO_2-containing air for 15 min compared to CO_2-free air at 600 °C.[26] After switching back to pure air, polarization resistances still remain over 2 times higher than the original ones due to the formation of a surface (Ba, Sr)CO_3 compound.[26] In theory, the average bonding energy (ABE) can be used to evaluate the stability of a material in different atmospheres. Taking $Sr_{1-x}Yb_xCoO_{3-\delta}$ as an example, with Co element on the B-site, calculations of Sr–O and Yb–O bonding energy in such ABO_3 perovskites are sufficient for their ABE comparison. Simple calculations indicate that the ABE of Yb–O, −119.45 kJ mol^{-1}, is more negative than that of Sr–O, *i.e.* −83.80 kJ mol^{-1}.[27] Therefore, it is reasonable to expect that partial substitution of Sr on the A-site by Yb may lead to less oxygen loss and better thermal stability at elevated temperatures, and may also improve stability in CO_2 containing atmospheres. In addition, Yb has a higher electronegativity value (~1.1) than Sr (1.0),[28] meaning that Yb has more power to attract electrons than Sr. Therefore, partial substitution of Sr with Yb on the A-site can decrease the basicity of the material and thus increase resistance against acidic gases.

In this research, a new series of $Sr_{1-x}Yb_xCoO_{3-\delta}$ (x = 0.05, 0.10 and 0.15) was synthesized and characterized including crystal structure evolution with Yb doping levels, oxygen reduction reaction kinetics and associated rate limiting steps, thermal stability, and stability in a CO_2-containing atmosphere at elevated temperatures.

2. Experimental procedures

2.1 Powder synthesis

$Sr_{1-x}Yb_xCoO_{3-\delta}$ (x = 0, 0.05, 0.10 and 0.15, simply denoted as SYbC0, SYbC5, SYbC10 and SYbC15, respectively) powders were synthesized by a combined ethylenediaminetetraacetic acid (EDTA)–citric acid complexing sol–gel process. Specifically, stoichiometric amounts of $Sr(NO_3)_2$ (Alfa Aesar, 99.0%), Yb_2O_3 (Alfa Aesar, 99.99%) and $Co(NO_3)_2 \cdot 6H_2O$ (Alfa Aesar, 99.999%) were dissolved in diluted nitric acid. After a transparent solution formed under magnetic stirring, citric acid (99.0–102.0%, BDH) and EDTA (99.4–100.6%, BDH) were added into the solution as complexants at a molar ratio of citric acid : EDTA : metal ions = 1.5 : 1 : 1. The pH value of the solution was adjusted to about 8 by adding ammonium hydroxide. After being mixed homogeneously, the precursor solution was heated in a water bath at 80 °C to evaporate excess water until a viscous gel was obtained. An electrical burner was then used to heat the gel until it self-burned, forming a bouffant ash. The resulting precursor powder was ground and then calcined at 400 °C for 2 h to remove organic residues, and then at 1000 °C in air for 6 h to form the $Sr_{1-x}Yb_xCoO_{3-\delta}$ (denoted as SYbCx) phase, followed by high energy ball milling for 1 h with ethanol as a milling medium.

2.2 Symmetrical cell preparation

To characterize the electrochemical performance of the synthesized SYbCx materials, symmetrical cells with the configuration SYbCx/$Ce_{0.8}Sm_{0.2}O_{1.9}$/SYbCx were fabricated. $Ce_{0.8}Sm_{0.2}O_{1.9}$ (SDC) electrolyte powder (tape cast grade, Fuel

 This journal is © The Royal Society of Chemistry 2020

Published on 04 May 2020. Downloaded by University of South Carolina Libraries on 5/18/2020 1:19:33 PM.

Cell Material, USA) was mixed and ground with binder polyvinyl butyral (PVB, 2 wt%) in ethanol. After being completely dried, the powder was uniaxially pressed at around 200 MPa using a stainless steel die to form a disk with a diameter of ~15 mm. Green pellets were then sintered and densified at 1450 °C in air for 6 h. The surfaces of the densified SDC pellets were polished with sandpaper and then cleaned in ethanol in an ultrasonic cleaner. SYbC*x* cathode powders were mixed with a balanced amount of 6 wt% ethyl cellulose–terpineol binder to form a cathode ink, which was then screen-printed onto both sides of each SDC pellet. After drying and aging, the symmetrical cells were sintered at 1050 °C in air for 2 h. Silver paste and wire were attached at either surface of electrodes as current collectors.

2.3 Characterization

X-ray diffraction (XRD, D/MAX-3C) with Cu Kα radiation (λ = 1.5406 Å) was employed to characterize the phase purity and crystal structure of powder materials at room temperature. XRD data were collected over a 2θ range from 10° to 90° with a step size of 0.02°. Rietveld refinements were performed on XRD patterns of SYbC5 and SYbC10, respectively, with GSAS-II/EXPGUI software.[29] Transmission electron microscopy (TEM) measurements were performed on a Hitachi H-9500 TEM with an accelerating voltage of 300 kV. To prepare samples for TEM measurements, nanoparticle samples were diluted in ethanol and sonicated for 30 min to ensure a homogeneous distribution of particles. Two drops of the suspension were deposited onto a carbon stabilized formvar-coated copper grid and completely dried at room temperature prior to measurement. The microstructure of the prepared samples was characterized with a scanning electron microscope (SEM, Zeiss Ultra Plus FESEM, Germany).

Electrochemical impedance spectroscopy (EIS) of symmetrical cells with SYbC5 and SYbC10 as electrode materials was performed using a Zahner IM6E electrochemical workstation under open circuit voltage in the frequency range from 10^6 to 0.1 Hz with a voltage perturbation of 10 mV. To further investigate the kinetics of the oxygen reduction reaction of the cathode material, polarization resistances at different oxygen partial pressures ($p(O_2)$) and different temperatures were measured. Various $p(O_2)$ were obtained by adjusting the flow rate ratio of oxygen *vs.* nitrogen, controlled by flow meters (APEX). Oxygen and nitrogen were supplied to a three-way valve through two individual lines and mixed. The mixed oxygen/nitrogen gas then flowed into a surge flask before entering the alumina test chamber.

The stability of the synthesized material as a cathode material was characterized, including crystal structure stability and long-term stability, as well as stability in a CO_2-containing atmosphere. In particular, to examine thermal stability, powders were annealed at 700 °C in air for 250 h, followed by XRD characterization. The long-term stability of SYbC10 as a cathode material was characterized at 700 °C in air for ~300 h, during which the polarization resistance of the symmetrical cell SYbC10/SDC/SYbC10 was measured periodically. The CO_2 tolerance and recovery capability of SYbC10 as a cathode material were also characterized using a symmetrical cell at 700 and 650 °C, respectively. The atmosphere surrounding the symmetrical cell was switched periodically between pure air and 5% CO_2–air. The polarization resistance of the symmetrical cell was measured every half hour.

3. Results and discussion

3.1 Crystal structure characterization and analysis of the as-prepared $Sr_{1-x}Yb_xCoO_{3-\delta}$ powders

The synthesis of a perovskite material usually starts from precursor powder preparation, followed by calcination at elevated temperatures to form a desired crystal phase. After cooling down, the phase formed at elevated temperatures is kept at room temperature. Unfortunately, undoped strontium cobalt oxide loses lattice oxygen at elevated temperature, forming $Sr_2Co_2O_5$ as described by reaction (1). During the cooling down process, $Sr_2Co_2O_5$ absorbs oxygen from air, forming $Sr_6Co_5O_{15}$ and Co_3O_4 as expressed by reaction (2).[30–33]

$$2SrCoO_{3-\delta} \leftrightarrow Sr_2Co_2O_5 + \frac{(1-2\delta)}{2}O_2 \quad (1)$$

$$3Sr_2Co_2O_5 + \frac{2}{3}O_2 \leftrightarrow Sr_6Co_5O_{15} + \frac{1}{3}Co_3O_4 \quad (2)$$

As shown in Fig. 1, the XRD pattern of our synthesized undoped $SrCoO_{3-\delta}$ does indeed consist of $Sr_6Co_5O_{15}$ and Co_3O_4, confirming that it is very difficult to synthesize a pure $SrCoO_{3-\delta}$ phase. Interestingly, upon substitution of Sr by Yb, the material phase is stabilized and exhibits a higher symmetry perovskite

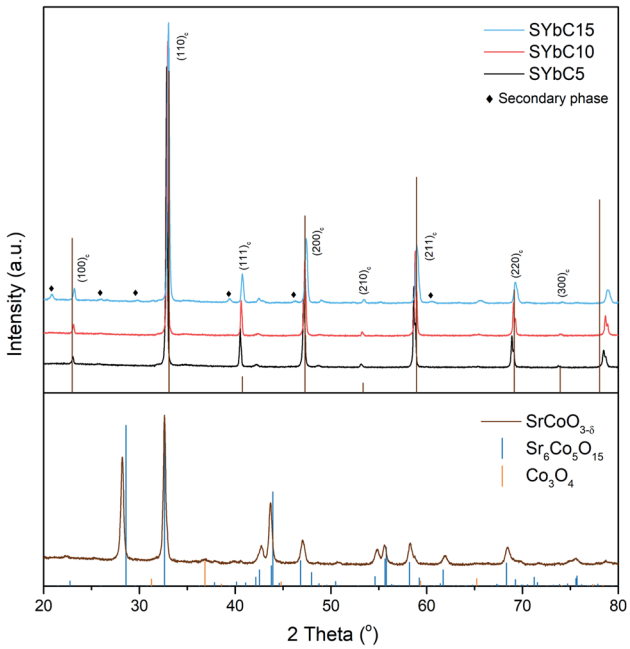

Fig. 1 XRD patterns of $Sr_{1-x}Yb_xCoO_{3-\delta}$ (x = 0, 0.05, 0.10 and 0.15) powders calcined at 1000 °C in air for 6 h; peak positions of $Sr_6Co_5O_{15}$, and Co_3O_4 and indices of simple cubic structure $SrCoO_{3-\delta}$ ($Pm\bar{3}m$, JCPDS 38-1148).

Published on 04 May 2020. Downloaded by University of South Carolina Libraries on 5/18/2020 1:19:33 PM.

phase. It is easy to see that SYbC5 and SYbC10 powders are well crystallized to a single phase, respectively. With increasing the Yb doping level to 15 mol%, secondary phase peaks appear in the SYbC15 XRD patterns (Fig. 1), implying that a 10 mol% doping level seems to be the upper limit for Yb solubility on the A-site of $SrCoO_{3-\delta}$. Using the basis of a cubic structure (JCPDS 38-1148), the indices of diffraction peaks of SYbC5 and SYbC10 are marked in Fig. 1, indicating that the main features of the XRD patterns could be explained by the cubic phase with the perovskite structure. Accordingly, these materials exhibit a higher symmetry structure of the perovskite phase upon A-site partial substitution of Sr by Yb.

Fig. 2a shows magnified XRD patterns of SYbC5 and SYbC10 in the range of $2\theta = 38°–56°$. One can see that some small peaks appear at 42° and 48.5° in the diffraction patterns. The magnified XRD patterns around $(200)_c$, $(211)_c$, and $(220)_c$ in Fig. 2b demonstrate increasingly obvious peak splitting of the XRD patterns. It is not straightforward to interpret either additionally appearing small peaks or peak splitting based on the understanding of the cubic crystal structure. The peak variations could be related to the distribution of oxygen vacancies in the crystal structure; for instance, oxygen vacancies in the perovskite phase are not completely disordered and vacancy ordering can appear locally.[34] In fact, upon oxygen vacancy ordering, tetragonal superstructures (*I*4/*mmm*) can occur in Co-based perovskites, and have the following relationship with the corresponding unit cell:

$$a_t \times a_t \times c_t \approx 2a_c \times 2a_c \times 4a_c \quad (3)$$

where a_t and c_t are lattice parameters of the tetragonal structure, while a_c is one of the corresponding primitive cubic unit cells.[35,36] The two additional small peaks at 42° and 48.5° could originate from the supercell formed upon vacancy ordering, which can also explain the splitting of the peaks.[34] Thus, more than likely, the structures of SYbC5 and SYbC10 are tetragonal with oxygen ordering vacancies instead of cubic perovskite with disordered vacancies. With increasing Yb content from 5 to 10 mol%, the two small peaks at 42° and 48.5° become less pronounced, indicating dissolution of the oxygen-ordered superlattice into an oxygen-disordered primitive cubic structure. Seemingly, a structural transition takes place from tetragonal towards cubic. In the meantime, the peaks shift to higher angles as shown in Fig. 2, indicating that such a structural transition is accompanied by lattice shrinkage.

To further understand XRD data and examine the above analysis, Rietveld refinement was performed on these experimental XRD patterns of SYbC5 and SYbC10 by using the GSAS-II program, where the tetragonal structure with the *I*4/*mmm* space group was used as an initial model. Fig. 3a and b show the refinement results of the XRD patterns for SYbC5 and SYbC10, respectively. Table 1 lists the details of fitting and structural parameters. A reasonable low weighted profile *R*-factor (R_{wp}), integrated intensity *R*-factor (R_F^2) and goodness of fit (χ^2) are achieved when the tetragonal *I*4/*mmm* space group is used to fit the experimental XRD data. And a good agreement was achieved between the XRD profile and the fitting results as graphically shown in Fig. 3, which ensures a good quality for Rietveld refinement. It can also be observed that partial substitution of Sr by Yb leads to smaller lattice and cell volumes, which is consistent with the XRD peak shifting in Fig. 2. With increasing Yb-doping levels from 5 to 10 mol%, the corresponding $c_t/2a_t$ ratio gradually approaches 1, leading to a structural transition tendency towards a cubic lattice. This result is also consistent with the above analysis of crystal structure evolution. Schematics of the crystal structures of SYbC0 and SYbC10 are shown in Fig. S1 (ESI).†

A transmission electron microscope (TEM) was employed to further characterize the crystal structures of SYbC5 and SYbC10. Fig. 4a and b show the micro-morphology of SYbC5 and SYbC10 powders, respectively. More TEM images of SYbC10 powders are provided in Fig. S2.† It can be seen that the powders consist of both large particles and small spherical particles. Small spherical particles with a diameter of ~2 to 3 nm can be observed (see the dashed circles in Fig. 4 and S2†). Additionally, some larger particles are formed with the aggregation of small spherical particles (Fig. S2†). High-resolution TEM images of selected regions of SYbC5 and SYbC10 exhibit well-defined crystalline fringes as shown in Fig. 4c and d, respectively. Interplanar

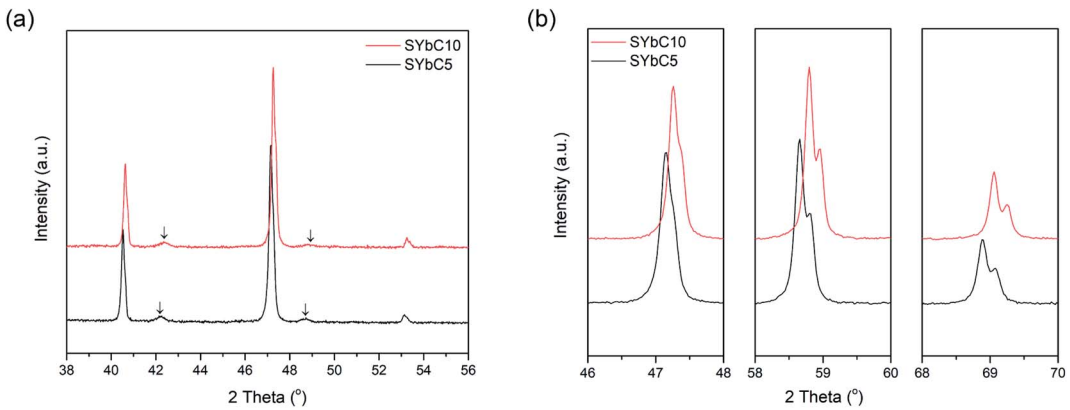

Fig. 2 Magnified XRD patterns of SYbC5 and SYbC10 powders calcined at 1000 °C in air for 6 h: (a) $2\theta = 38°–56°$; (b) $(200)_c$, $(211)_c$, and $(220)_c$ peaks.

 This journal is © The Royal Society of Chemistry 2020

Published on 04 May 2020. Downloaded by University of South Carolina Libraries on 5/18/2020 1:19:33 PM.

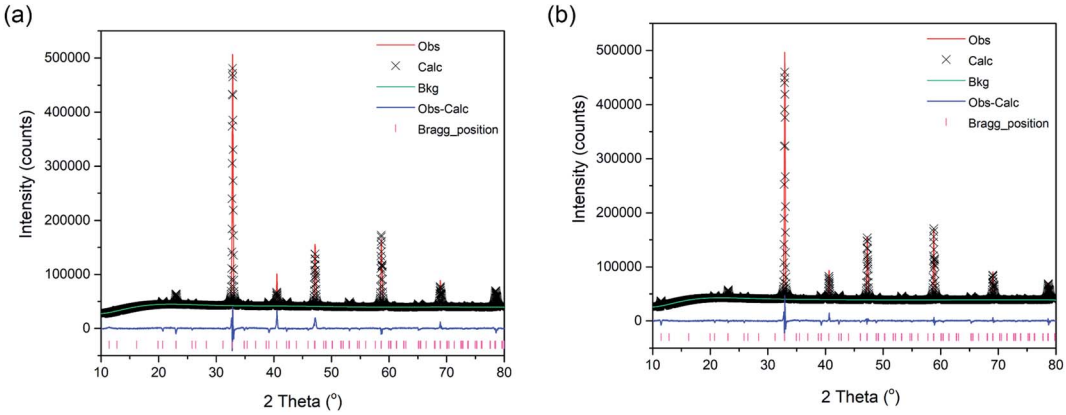

Fig. 3 Rietveld refinement plot of SYbC5 (a) and SYbC10 (b) powders at room temperature using XRD data.

Table 1 Structural parameters and R-factors for SYbC5 and SYbC10 derived from Rietveld refinement using XRD data at room temperature

	$x = 0.05$	$x = 0.10$
a_t (Å)	7.6944(7)	7.6813(0)
c_t (Å)	15.4117(7)	15.3809(7)
$c_t/2a_t$	1.00147(9)	1.00119(5)
V (Å^3)	912.453	907.513
χ^2	6.29	4.67
R_{wp} (%)	3.01	2.26
$R_F{}^2$ (%)	6.02	2.63

distances of 0.283 nm and 0.258 nm were obtained from the fringe measurements for SYbC5 and SYbC10, respectively, which is related to the $(220)_t$ or $(110)_c$ lattice plane as shown in Fig. S3.† Although interplanar distances obtained from these TEM images show a slight difference from the above Rietveld refinement result due to measurement and fitting errors, the variation tendencies of the lattice parameters are consistent with each other. All of these results suggest that partial substitution of Sr with 5 and 10 mol% Yb on the A-site leads to an evolution of the corresponding lattice structure and is able to stabilize the high temperature phase of $SrCoO_{3-\delta}$ to room temperature.

3.2 Structural stability of the synthesized powders after thermal treatment

SOFCs operate at elevated temperatures and require long-term stability of the involved materials, in particular, the cathode materials. The purpose of the partial substitution of Sr with Yb in $SrCoO_{3-\delta}$ mentioned above is to stabilize the high temperature crystal structure down to room temperature, so that crystal structure stability can be obtained in a wide operating temperature range. In this section, the thermal stability of the synthesized powders of SYbC5 and SYbC10 is evaluated. In particular, the as-prepared SYbC5 and SYbC10 powders were annealed at 700 °C in air for 250 h. The XRD patterns of the powders before and after annealing treatment were obtained. As shown in Fig. 5, the materials maintained the same crystal structures before and after annealing treatment, indicating that both SYbC5 and SYbC10 powders are thermally stable at 700 °C in air.

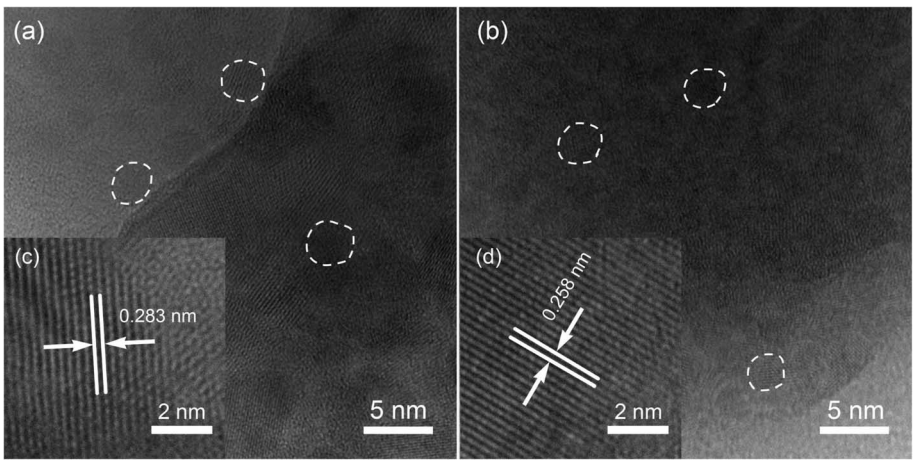

Fig. 4 High-resolution TEM images of SYbC5 (a) and SYbC10 (b) powders after high energy ball milling and interplanar distance of SYbC5 (c) and SYbC10 (d) powders.

Published on 04 May 2020. Downloaded by University of South Carolina Libraries on 5/18/2020 1:19:33 PM.

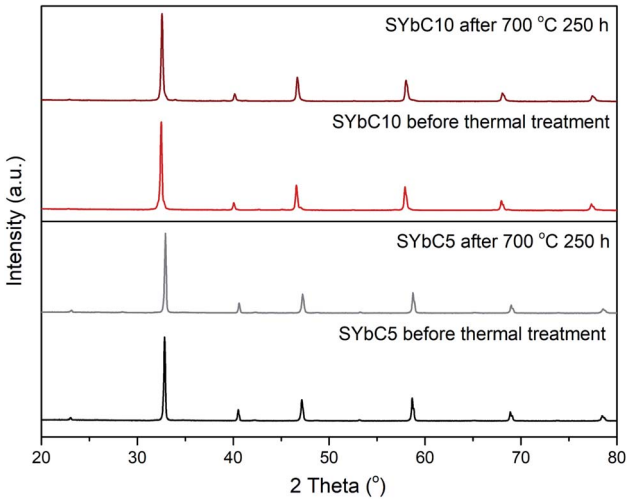

Fig. 5 XRD patterns of SYbC5 and SYbC10 powders before and after annealing treatment at 700 °C in air for 250 h.

3.3 Electrochemical performance and stability of SYbC5 and SYbC10 as electrode materials

3.3.1 Yb doping effect on polarization resistances of SYbC5 and SYbC10 cathodes. To evaluate the Yb dopant effect on the electrochemical performance of SYbC5 and SYbC10, the polarization resistance (R_p) was measured on symmetrical cells using EIS under open circuit voltage conditions in the temperature range of 600–750 °C. SEM images (Fig. S4†) show that SYbC5 and SYbC10 cathodes demonstrate intimate contact with SDC electrolyte and have sufficient porosity; the sintered particles also show good inter-connectivity throughout the cathode.

Fig. 6 shows typical EIS of SYbC5 and SYbC10 electrodes measured at 700 °C in air. Spectral fitting results are shown in the same figure using an equivalent circuit with the configuration L–R_o–(R_hQ_h)–(R_lQ_l) (inset in Fig. 6a), where L denotes the inductance of the circuit, R_o represents the ohmic resistance induced by the electrolyte and electrode backbone as well as current collecting wires, and R_i and Q_i are the resistance and constant phase capacitance of high (h) and low (l) frequency processes, respectively. The fitting results of R_h and R_l are corrected by the electrode area and divided by two because of the symmetrical configuration of the cell. The polarization resistance of the electrode (R_p) is then obtained by adding R_h and R_l together. The Bode plot in Fig. 6b shows the frequency response of the imaginary part of the impedance spectra, indicating that the improved performance of the SYbC10 electrode is mainly associated with low frequency processes. The Arrhenius plots of R_p of SYbC5 and SYbC10 electrodes at different temperatures and the corresponding activation energy (E_a) are presented in Fig. 7. Obviously, R_p decreases with increasing temperature, indicating that electrochemical processes occurring in the electrode are thermally activated. Increasing the amount of Yb dopant from 5 to 10 mol% results in a decrease in R_p. The SYbC10 electrode shows polarization resistances of 0.051, 0.115 and 0.272 Ω cm^2 at 750, 700 and 650 °C, respectively, lower than those of the SYbC5 electrode. The activation energy of SYbC10 is 1.39 eV, which is also lower than that of the SYbC5 electrode, that is 1.57 eV. This could be attributed to crystal structure evolution induced by the Yb dopant. As mentioned previously, with increasing doping content of Yb from 5 to 10 mol%, a gradual structural transition took place from the tetragonal structure with oxygen vacancy

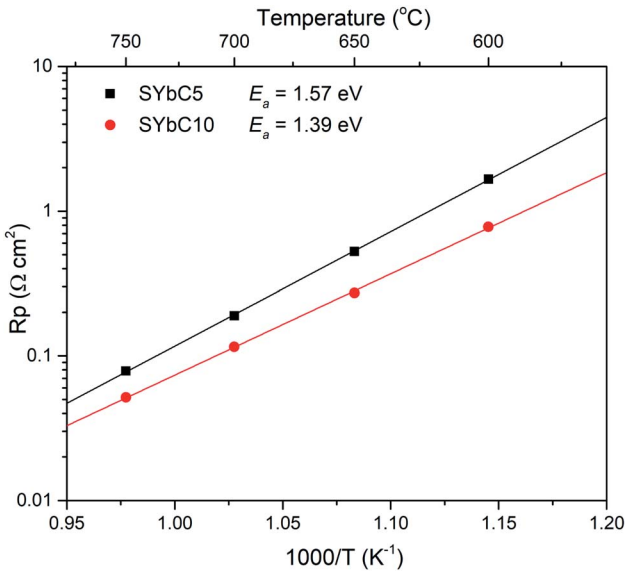

Fig. 7 Polarization resistance *vs.* 1000/*T* of SYbC5 and SYbC10 electrodes measured in air from 750 to 600 °C.

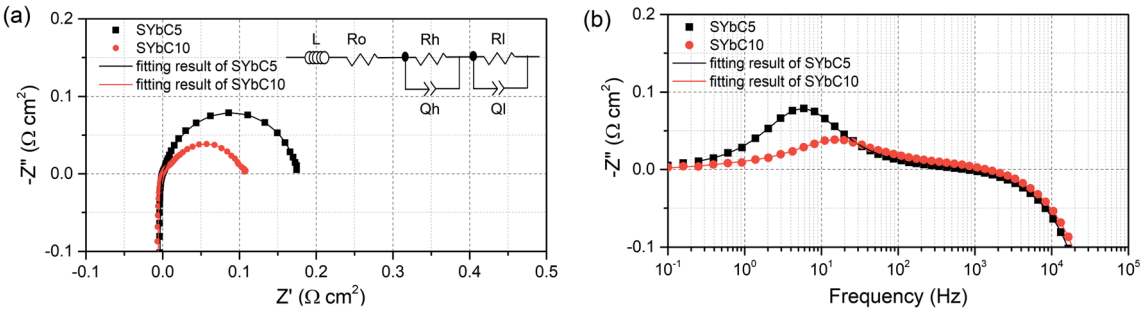

Fig. 6 Typical Nyquist (a) and Bode (b) plots of symmetrical cells with SYbC5 and SYbC10 electrodes measured at 700 °C in air. The inset is an equivalent circuit model used for curve fitting.

 This journal is © The Royal Society of Chemistry 2020

Published on 04 May 2020. Downloaded by University of South Carolina Libraries on 5/18/2020 1:19:33 PM.

ordering towards disordered vacancies. Accordingly, SYbC10 possesses a structure similar to the ORR/OER active primitive cubic symmetry with disordered oxygen vacancies. This creates 3D pathways for oxygen ion transport, favoring electrode processes. The resulting lower R_p and E_a values obtained from the SYbC10 electrode, when compared to the SYbC5 electrode results, support this explanation.

3.3.2 Oxygen partial pressure dependent polarization resistance and electrochemical kinetics. The ORR in the porous SYbC10 electrode involves complicated multistep reactions. The reaction process is strongly dependent on oxygen pressures applied on the electrode and determines the electrode polarization resistance. Mathematically,

$$R_i = kP_{O_2}{}^{-m},\ i = h, l \tag{4}$$

where R is the polarization resistance, k is a constant, P_{O_2} is the oxygen partial pressure, m is the reaction order and quantitatively related to each of the multistep reactions as follows:

Step 1: molecular oxygen adsorption process onto the porous electrode surface ($m = 1$)

$$O_{2,g} + SYbC10(s) \leftrightarrow O_{2,ads}(SYbC10) \tag{5}$$

Step 2: dissociation of adsorbed molecular oxygen into atomic oxygen ($m = 0.5$)

$$O_{2,ads}(SYbC10) \leftrightarrow 2O_{ads}(SYbC10) \tag{6}$$

Step 3: charge transfer reaction for oxygen anion formation and incorporation into an oxygen vacancy ($m = 0.25$)

$$O_{ads}(SYbC10) + 2e^- + V_O^{\cdot\cdot} \leftrightarrow O_O^{\times} + SYbC10(s) \tag{7}$$

Fig. 8a shows the correlation between high frequency polarization and applied oxygen partial pressures at different temperatures. It can be seen that reaction orders (m) of 0.28, 0.23, 0.29, and 0.27 are obtained at 600, 650, 700, and 750 °C, respectively, which are close to 0.25, suggesting that high frequency polarization is mainly associated with the charge transfer reaction process. Values of reaction order m for low frequency polarization are 0.48, 0.60, 0.57 and 0.59, respectively (Fig. 8b), indicating that the low frequency polarization is mainly associated with the dissociation of adsorbed oxygen molecules into atomic oxygen. Accordingly, oxygen molecule dissociation and charge transfer processes are the two rate-limiting steps for the SYbC10 cathode material.

3.3.3 Electrochemical kinetic stability of the SYbC10 cathode. Durability is critical for practical applications of SOFC cathode materials. In this section, a durability test was carried out using a symmetrical cell with an SYbC10 electrode at 700 °C in air for ~300 h. EIS was performed periodically during the test. The polarization resistance R_p was then derived from the fitted EIS data as described in the previous section. Fig. 9a shows the time history of polarization resistances. It can be seen that R_p fluctuates in the first 50 hours, and then increases a little bit between 50 and 175 h. Beyond 175 h, R_p gradually approaches an equilibrium state. Fig. 9b shows EIS curves measured at the 0th, 52nd, 113th, 263rd, and 309th hours, respectively. The EIS arcs gradually increase with time and reach an equilibrium state by the end of the test. As mentioned above, the polarization resistance of the electrode is contributed by several steps in the ORR. This increase in electrode polarization resistance could be linked to specific ORR steps, through which the degradation mechanism of the electrode might be identified. For this purpose, the time history of high (R_h) and low (R_l) frequency polarization resistances was obtained from the EIS measurements and is shown in Fig. 10a and b, respectively. R_h shows some scatters in the first 100 hours, but gradually stabilizes and reaches a value comparable to (actually a little bit lower than) the values recorded at the start of the durability test. Since high frequency polarization is associated with the charge transfer process as confirmed above for oxygen anion formation and incorporation into an oxygen vacancy, it is reasonable to assume that the surface oxygen vacancy distribution and electronic structure near oxygen vacancies remain stable during the test. The fluctuations in the R_h data in the first 100 hours may be related to reorganization and stabilization of the oxygen vacancy distribution on the electrode surface. R_l also

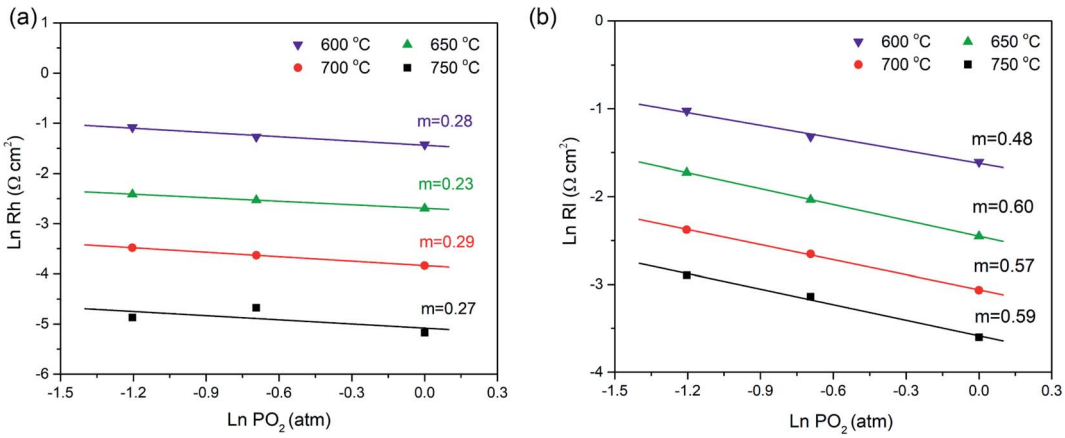

Fig. 8 Correlations between R_h (a), R_l (b) and applied oxygen partial pressures at different temperatures.

Published on 04 May 2020. Downloaded by University of South Carolina Libraries on 5/18/2020 1:19:33 PM.

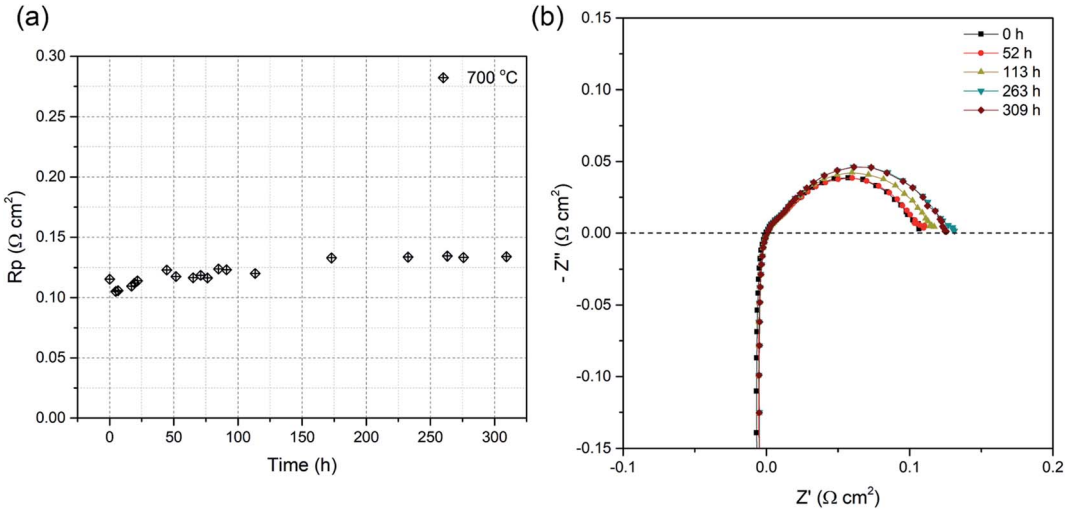

Fig. 9 Long-term stability of the SYbC10/SDC/SYbC10 symmetrical cell in air at 700 °C: (a) time history of polarization resistance, (b) evolution of EIS at selected measurement points.

fluctuates in the first 25 hours, but then slowly increases, and reaches a relatively stable value around the 300th h. As mentioned above, low frequency polarization resistance is closely related to the dissociation of adsorbed oxygen molecules into atomic oxygen. Certainly, the dissociation process is affected by the surface catalytic properties of the electrode, so it is reasonable to assume that the increase of R_l could be induced by a change in electrode surface characteristics. For ABO_3 perovskites, both A-site and B-site elements could be exsolved onto the bulk surface under long-term thermal treatment conditions.[23,37–41] As shown in Fig. 5, no secondary phase can be found in the XRD results of SYbC10 powders after 250 h thermal treatment, implying that either no element was exsolved from A-/B-sites or the extent of surface element exsolution was below the level detectable by XRD. On the other hand, surface nanoparticles are observed from the SEM image of the SYbC10 electrode after the durability test (Fig. S5b†), indicating that some elements were indeed exsolved. It has been widely demonstrated that transition metal exsolution from the B-site usually improves the catalytic properties or surface exchange rate of the material.[42,43] However, the increase of R_l shown in Fig. 10b indicates that this is less likely the case. Therefore, the surface nanoparticles in Fig. S5b† are most likely induced by element exsolution from the A-site. In $Sr_{1-x}Yb_xCoO_{3-\delta}$, the size mismatch between dopant and host cations induces elastic energy in crystals. During the long-term thermal treatment process, such an elastic energy may drive cation rearrangement, resulting in surface Sr segregation. Ideal cubic $SrCoO_{3-\delta}$ consists of SrO and CoO_2 planes showing alternating stacking with $-(SrO–CoO_2)_n-$ sequences. The Sr and Co cations have charges of +2 and +4, respectively, leading to a neutral charge of $Sr^{2+}O^{2-}$ [0] and $Co^{4+}O_2{}^{2-}$ [0] planes. However, Yb with a charge of +3 leads to a positive charge of $Yb^{3+}O^{2-}$ [+1] in the AO planes and potential formation of negatively charged $Co^{3+}O_2{}^{2-}$ [−1] in the BO_2 planes. The alternating stacking of the charged AO and BO_2 planes would result in a polar surface, which in turn could

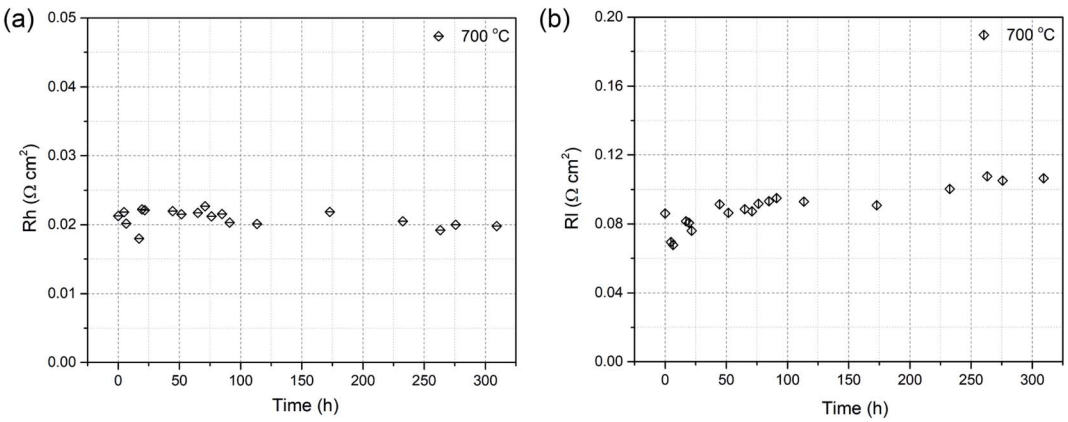

Fig. 10 Time history of polarization resistance associated with the high frequency (a) and low frequency (b) process for the SYbC10 cathode at 700 °C in air.

 This journal is © The Royal Society of Chemistry 2020

Published on 04 May 2020. Downloaded by University of South Carolina Libraries on 5/18/2020 1:19:33 PM.

electrostatically drive surface cation segregation. Due to the lower surface energy of the SrO surface,[44,45] a SrO-terminated surface is prone to be formed with segregated Sr. Therefore, surface Sr segregation of $Sr_{1-x}Yb_xCoO_{3-\delta}$ could be induced by both elastic force and electrostatic force during long-term thermal treatment. To maintain charge neutrality, surface oxygen vacancies will be created. This process can be expressed as

$$Sr_{Sr}^{\times} + O_O^{\times} \leftrightarrow V_{Sr}'' + V_O^{\cdot\cdot} + SrO_{surface} \quad (8)$$

The surface oxygen vacancies created *via* surface Sr segregation will improve the surface oxygen exchange rate and ORR kinetics. However, when the Sr segregation is beyond a certain level, it might block the neighboring oxygen vacancies and reaction sites.[46,47] This understanding may explain the time history of R_l. In the first 10 hours, R_l shows a rapid decrease likely due to a low extent of surface Sr segregation. Beyond approximately the 10th h, the extent of surface Sr segregation increases, leading to a gradual increase of R_l values. R_l stabilizes around the 300th h, implying that surface Sr segregation reaches an equilibrium state. It seems that the increase of overall polarization resistance R_p during the durability test is primarily induced by the increase of R_l, and therefore performance degradation could be mainly caused by surface Sr segregation.

3.3.4 CO_2 tolerance and recovery capability of the SYbC10 cathode. The gas supplied to the cathode electrodes of SOFCs may contain a small amount of CO_2, especially air from the surrounding ambient atmosphere. Even though the CO_2 content is very low, it may easily adsorb onto the cathode surface, forming several types of surface adsorbates. Surface adsorbed CO_2 could even react with a cathode material, resulting in surface secondary phases.[48] This usually occurs for Sr containing perovskite cathodes, where surface oxo-carbonaceous species, such as adventitious-like carbon species, monodentate carbonate, bidentate carbonate and carbonate species, are formed at elevated temperatures.[49,50] Such surface oxo-carbonaceous species block ORR active sites and cause deterioration of surface (electro)catalytic properties, causing degradation of cathode electrodes. Although degradation alleviation is possible by annealing at a relatively high temperature, *e.g.* decomposition of $SrCO_3$ in air[51,52] and desorption of surface oxo-carbonaceous species, the high temperature process may induce other problems such as microstructure coarsening of electrodes and unwanted side reactions at interfaces within the device, which make it difficult for the device to recover its initial state and performance. In this section, the stability and recovery capability of SYbC10 as a cathode material is evaluated using a symmetrical cell in a CO_2-containing atmosphere at elevated temperatures. For this test, a symmetrical cell, SYbC10/SDC/SYbC10, was sealed in an alumina tube chamber. Pure air and 5% CO_2-containing air were supplied into the chamber alternatively every 2 hours for the first 12 hours. After 12 hours, pure air was constantly supplied into the chamber without switching to CO_2 containing air. EIS was performed every half hour during the testing. R_o and R_p were then extracted from the EIS data. Fig. 11 shows the time history of R_o and R_p at 700 and 650 °C, respectively. It can be seen that at 700 °C, the ohmic resistance remained stable for the first ~7 hours, then showed a small increase, and stayed unchanged for the remainder of the test (Fig. 11a). It did not show any obvious variations following the applied cycling between pure air and 5% CO_2–air. This observation indicates that variations in R_o are mainly induced by the thermal ageing process, in which the cell may experience microstructure evolution during the course of the stability test at 700 °C. The polarization resistance in Fig. 11b clearly shows fluctuations that followed the applied cycles of the surrounding gas atmosphere. R_p was relatively low in pure air but quickly increased to a high value once the gas atmosphere was switched to 5% CO_2–air. This result indicates that the SYbC10 material is very sensitive to CO_2 but reversible from the CO_2-contaminated state. Interestingly, after a few gas cycles, R_p becomes lower than the initial value, implying that a surface phase/microstructure beneficial for the electrocatalytic properties of the electrode could be formed, which is not completely clear at this stage. In addition to potential adsorption/desorption of surface carbonaceous species, it is assumed that the following surface reactions are occurring:

$$Sr_{0.9}Yb_{0.1}CoO_{3-\delta} + xCO_2 \rightarrow xSrCO_3 + Sr_{0.9-x}Yb_{0.1}CoO_{3-\delta} \text{ (in 5\% } CO_2 \text{ containing air)} \quad (9)$$

$$SrCO_3 + O_2 \rightarrow SrO + CO_2 \text{ (in pure air)} \quad (10)$$

At a temperature of 700 °C, Sr segregation first occurs and Sr appears on the cathode surface. When CO_2 is adsorbed onto the cathode surface, the surface segregated Sr and/or lattice Sr is converted into $SrCO_3$ (reaction (9)). Fig. S6† shows the XRD patterns of SYbC10 powders after being treated in 5% CO_2–air for 2 h at 650 and 700 °C, respectively, followed by cooling down under the protection of nitrogen gas. It can be seen that the peaks corresponding to the $SrCO_3$ phase appeared. This result confirms the assumption that CO_2 did react with Sr in SYbC10, forming the $SrCO_3$ phase. After switching to pure air, the chemisorbed surface carbonaceous species are desorbed and the formed $SrCO_3$ is decomposed into SrO and CO_2 at 700 °C (reaction (10)). In fact, after SYbC10 powders were treated at 700 °C in 5% CO_2–air for 2 h followed by treatment in pure air for another 2 h at 700 °C, the $SrCO_3$ phase completely disappeared but the SrO phase appeared as shown in Fig. S7.† After a few gas cycles, the nanoporous surface and/or surface micro-composition that favors the ORR on the electrode may be formed, leading to smaller values of R_p. At a lower temperature of 650 °C, the variations in ohmic resistance synchronize with the cycles of applied gas atmosphere (Fig. 11c). Interestingly, R_o was slightly larger during the pure air portion of the cycle than in the 5% CO_2–air portion of the cycle. Variation in polarization resistance also followed the cycles of applied gas atmosphere, low in the pure air cycle but high in the 5% CO_2–air cycle (Fig. 11d). While R_p remained relatively constant in pure air after the first gas cycle, in 5% CO_2–air, it increased by ~350% of

Published on 04 May 2020. Downloaded by University of South Carolina Libraries on 5/18/2020 1:19:33 PM.

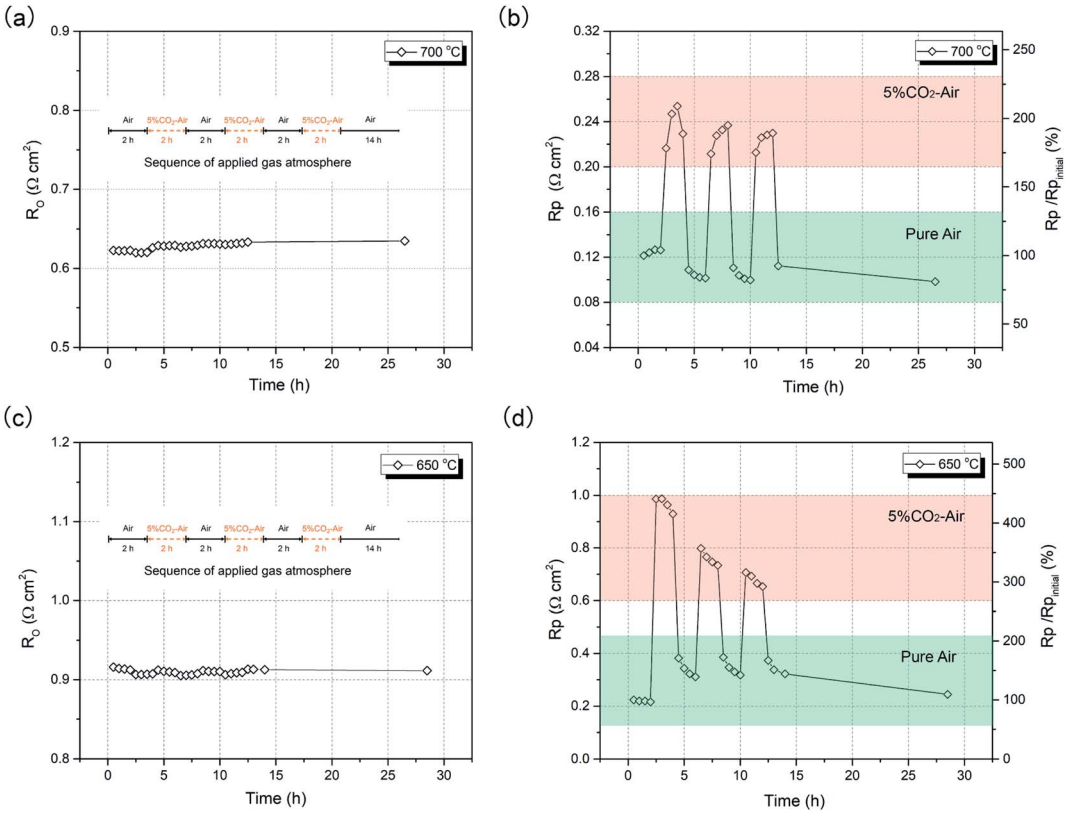

Fig. 11 Time history of ohmic and polarization resistance evolution curves of the SYbC10 electrode in applied gas cycles between air and 5% CO_2–air at 700 (a and b) and 650 °C (c and d).

its initial value, but began decreasing every subsequent gas cycle. After air treatment, R_p at the 28th h showed a little higher value than its initial one before the cycling test.

Based on the above analysis and experimental results, one can see that R_p variations of the SYbC10 electrode are attributed to two major surface factors during the atmosphere switching between pure air and 5% CO_2–air: one is surface oxo-carbonaceous species, *e.g.* adventitious-like carbon and (bi) carbonate species, induced by direct chemisorption of CO_2; the other is the surface $SrCO_3$ phase formed by chemical reaction of Sr and CO_2. At elevated temperatures, the SYbC10 electrode will lose oxygen and generate more oxygen vacancies. It has been reported that surface oxygen vacancies are the acidic centers for the adsorption of CO_2.[53] This may lead to more CO_2 reacting with surface Sr, forming the $SrCO_3$ phase in 5% CO_2–air since perovskite with more oxygen vacancies is more susceptible to CO_2.[54] It is reasonable to assume that the amount of $SrCO_3$ phase formed at 700 °C will be more than that at 650 °C. This understanding is confirmed by XRD results in Fig. S6,† where after SYbC10 powders were treated in 5% CO_2–air for 2 h at 650 and 700 °C, respectively, the secondary phase of $SrCO_3$ was formed. And the relative peak intensity of $SrCO_3$ at 700 °C is stronger than that at 650 °C, indicating that the formation of strontium carbonates is more favored at higher temperatures for SYbC10. On the other hand, it has been recognized that surface oxo-carbonaceous species, *e.g.* adventitious-like carbon and (bi)carbonate species, are favorably chemisorbed at lower temperatures.[49] In other words, it is difficult to desorb such surface oxo-carbonaceous species at lower temperatures. Both the formed surface strontium carbonate and chemisorbed surface oxo-carbonaceous species will block reaction sites for surface oxygen exchange. Since the formed surface strontium carbonate and chemisorbed surface oxo-carbonaceous species are sensitive to operating temperatures, the combinational effect of these two surface factors leads to different R_p behaviors at 650 °C from those at 700 °C. This could be the reason that the increase of R_p (or the increased ratio of R_p relative to its initial value) at 650 °C is larger than that at 700 °C when the atmosphere is switched from pure air to 5% CO_2–air (Fig. 11). After the atmosphere is switched from 5% CO_2–air back to pure air, R_p at 700 °C rapidly recovers and reaches a value that is a little bit lower than its initial one (Fig. 11b). This result implies that not only the chemisorbed surface carbonaceous species are completely desorbed but also the formed surface strontium carbonates are fully decomposed. Meanwhile, the decomposition of surface strontium carbonates might also introduce porous nano-surface structures favoring the ORR. By contrast, R_p at 650 °C shows only partial recovery and reaches a value that is higher than its initial one (Fig. 11d). This observation indicates that the chemisorbed surface oxo-carbonaceous species are not completely desorbed and/or the formed surface strontium carbonates are not completely decomposed at 650 °C after the atmosphere is changed back to pure air from 5% CO_2–air. As a consequence, the surface ORR sites of SYbC10 electrodes are

 This journal is © The Royal Society of Chemistry 2020

Published on 04 May 2020. Downloaded by University of South Carolina Libraries on 5/18/2020 1:19:33 PM.

still partially blocked. The non-complete recovery of ORR sites also leads to a hysteresis behavior in the cell resistance at 650 °C during the atmosphere cycles between pure air and 5% CO_2–air. In the open literature, the R_p of the widely studied $Ba_{0.5}Sr_{0.5}Co_{0.8}Fe_{0.2}O_{3-\delta}$ (BSCF)[26] may reach 9 times its initial value after being exposed to 10% CO_2 for 15 min at 700 °C, and 27 times its initial value after being exposed to 5% CO_2 for 15 min at 600 °C. The maximum R_p of SYbC10 achieved in this paper only reached ~2.1 times (Fig. 11b) and 4.5 times (Fig. 11d) at 700 °C and 650 °C, respectively, after being exposed to 5% CO_2 for 30 min. This simple comparison indicates that SYbC10 has good properties for CO_2 tolerance. The partial substitution of Sr by Yb with higher electronegativity on the A-site is able to mitigate CO_2 adsorption onto the SYbC10 electrode surface.

4. Conclusion

A new series of $Sr_{1-x}Yb_xCoO_{3-\delta}$ ($x = 0$, 0.05, 0.10 and 0.15) with different Yb doping concentrations has been synthesized and systematically characterized. The results indicate that $Sr_{0.95}Yb_{0.05}CoO_{3-\delta}$ and $Sr_{0.90}Yb_{0.10}CoO_{3-\delta}$ samples possess a tetragonal superstructure phase with oxygen vacancy ordering (*I*4/*mmm*; $2a_c \times 2a_c \times 4a_c$). With increasing the Yb doping level, the phases demonstrate a transition tendency towards a cubic structure with disordered oxygen vacancies. Both SYbC5 and SYbC10 phases show excellent thermal stability at 700 °C. Due to the less ordered oxygen vacancies, SYbC10 demonstrates very good ORR activity with polarization resistances of 0.051, 0.115 and 0.272 Ω cm^2 at 750, 700 and 650 °C, respectively. Dissociation of adsorbed oxygen and charge transfer are the two rate-limiting steps in the ORR for the SYbC10 cathode. Durability testing (~300 h) in combination with EIS analysis indicates that the surface oxygen vacancy distribution and electronic structure near oxygen vacancies are very stable but dissociation of adsorbed oxygen molecules into atomic oxygen is affected by surface Sr segregation, and polarization resistance degradation is mainly induced by surface Sr segregation. SYbC10 is very sensitive to CO_2 containing atmospheres. At a relatively high temperature of 700 °C, the polarization resistance closely follows the cycles between pure air and CO_2–air and has relatively higher values during the CO_2–air portion of the cycle. This effect is temporary and polarization performance completely recovers in the pure air cycle, likely due to complete desorption of surface oxo-carbonaceous species and decomposition of surface carbonates. The polarization resistance after a few gas cycle treatments becomes lower than that before the CO_2 treatment, probably due to surface nanostructures induced by cyclic formation and decomposition of surface carbonates. At a relatively low temperature of 650 °C, the polarization resistance still follows the same cyclic behavior, but complete recovery from the CO_2–air portion of the cycle is not observed, leading to hysteresis behavior likely due to non-complete desorption of surface oxo-carbonaceous species and/or non-complete decomposition of surface carbonates after switching to the pure air portion of the cycle. After a few pure air to 5% CO_2–air cycles at 650 °C, the polarization resistance of the SYbC10 electrode increases from the initial value in pure air. This work provides a promising strategy to stabilize $SrCoO_{3-\delta}$ through a simple cation doping method while obtaining very good electrochemical kinetic properties and stability of the material. The material developed in this study can be used as an alternative cathode for intermediate temperature SOFCs toward commercial applications.

Conflicts of interest

There are no conflicts to declare.

Acknowledgements

This work was supported by the U.S. Department of Energy through the National Energy Technology Laboratory under contract numbers DE-FE0031473 and DE-FE0024059.

References

1 D. J. Brett, A. Atkinson, N. P. Brandon and S. J. Skinner, *Chem. Soc. Rev.*, 2008, **37**, 1568–1578.
2 E. D. Wachsman and K. T. Lee, *Science*, 2011, **334**, 935–939.
3 N. Q. Minh, *J. Am. Ceram. Soc.*, 1993, **76**, 563–588.
4 T. Komatsu, R. Chiba, H. Arai and K. Sato, *J. Power Sources*, 2008, **176**, 132–137.
5 J. Richter, P. Holtappels, T. Graule, T. Nakamura and L. J. Gauckler, *Monatsh. Chem.*, 2009, **140**, 985–999.
6 A. F. Sammells, R. L. Cook, J. H. White, J. J. Osborne and R. C. MacDuff, *Solid State Ionics*, 1992, **52**, 111–123.
7 D. Chen, C. Chen, Z. Zhang, Z. M. Baiyee, F. Ciucci and Z. Shao, *ACS Appl. Mater. Interfaces*, 2015, **7**, 8562–8571.
8 C. De la Calle, A. Aguadero, J. Alonso and M. Fernández-Díaz, *Solid State Sci.*, 2008, **10**, 1924–1935.
9 H. Kruidhof, H. J. Bouwmeester, R. v. Doorn and A. Burggraaf, *Solid State Ionics*, 1993, **63**, 816–822.
10 W. Zhou, Z. Shao, R. Ran and R. Cai, *Electrochem. Commun.*, 2008, **10**, 1647–1651.
11 R. D. Shannon, *Acta Crystallogr., Sect. A: Cryst. Phys., Diffr., Theor. Gen. Crystallogr.*, 1976, **32**, 751–767.
12 D. Chen, C. Chen, Y. Gao, Z. Zhang, Z. Shao and F. Ciucci, *J. Power Sources*, 2015, **295**, 117–124.
13 F. Wang, Q. Zhou, T. He, G. Li and H. Ding, *J. Power Sources*, 2010, **195**, 3772–3778.
14 W. Zhou, J. Sunarso, M. Zhao, F. Liang, T. Klande and A. Feldhoff, *Angew. Chem., Int. Ed.*, 2013, **52**, 14036–14040.
15 Y. Shen, F. Wang, X. Ma and T. He, *J. Power Sources*, 2011, **196**, 7420–7425.
16 A. Aguadero, J. A. Alonso, D. Pérez-Coll, C. de la Calle, M. a. T. Fernández-Díaz and J. B. Goodenough, *Chem. Mater.*, 2009, **22**, 789–798.
17 A. Aguadero, D. Pérez-Coll, J. Alonso, S. Skinner and J. Kilner, *Chem. Mater.*, 2012, **24**, 2655–2663.
18 M. Li, W. Zhou, V. K. Peterson, M. Zhao and Z. Zhu, *J. Mater. Chem. A*, 2015, **3**, 24064–24070.
19 G. López-Pacheco, R. López-Juárez, M. E. Villafuerte-Castrejón, C. Falcony, E. Barrera-Calva and F. González, *Dalton Trans.*, 2019, **48**, 11889–11896.

Published on 04 May 2020. Downloaded by University of South Carolina Libraries on 5/18/2020 1:19:33 PM.

20 Y. Wang, L. Li, J. Qi and Z. Gui, *Ceram. Int.*, 2002, **28**, 657–661.
21 S. W. Park, B. K. Moon, S. H. Park, J. H. Jeong, H. Choi and J. H. Kim, *RSC Adv.*, 2017, **7**, 1464–1470.
22 G. M. Rupp, A. K. Opitz, A. Nenning, A. Limbeck and J. Fleig, *Nat. Mater.*, 2017, **16**, 640.
23 Y. Li, W. Zhang, Y. Zheng, J. Chen, B. Yu, Y. Chen and M. Liu, *Chem. Soc. Rev.*, 2017, **46**, 6345–6378.
24 H. Yokokawa, H. Tu, B. Iwanschitz and A. Mai, *J. Power Sources*, 2008, **182**, 400–412.
25 M. Arnold, H. Wang and A. Feldhoff, *J. Membr. Sci.*, 2007, **293**, 44–52.
26 Y. Zhang, G. Yang, G. Chen, R. Ran, W. Zhou and Z. Shao, *ACS Appl. Mater. Interfaces*, 2016, **8**, 3003–3011.
27 H. Zhao, N. Xu, Y. Cheng, W. Wei, N. Chen, W. Ding, X. Lu and F. Li, *J. Phys. Chem. C*, 2010, **114**, 17975–17981.
28 W. Gordy and W. O. Thomas, *J. Chem. Phys.*, 1956, **24**, 439–444.
29 B. H. Toby and R. B. Von Dreele, *J. Appl. Crystallogr.*, 2013, **46**, 544–549.
30 R. Le Toquin, W. Paulus, A. Cousson, C. Prestipino and C. Lamberti, *J. Am. Chem. Soc.*, 2006, **128**, 13161–13174.
31 Y. Ito, R. F. Klie, N. D. Browning and T. J. Mazanec, *J. Am. Ceram. Soc.*, 2002, **85**, 969–976.
32 R. E. Usiskin, T. C. Davenport, R. Y. Wang, W. Guan and S. M. Haile, *Chem. Mater.*, 2016, **28**, 2599–2608.
33 W. T. Harrison, S. L. Hegwood and A. J. Jacobson, *J. Chem. Soc., Chem. Commun.*, 1995, 1953–1954.
34 T. Nagai, W. Ito and T. Sakon, *Solid State Ionics*, 2007, **177**, 3433–3444.
35 M. James, D. Cassidy, D. Goossens and R. Withers, *J. Solid State Chem.*, 2004, **177**, 1886–1895.
36 Y. Li, Y. N. Kim, J. Cheng, J. A. Alonso, Z. Hu, Y.-Y. Chin, T. Takami, M. T. Fernández-Díaz, H.-J. Lin and C.-T. Chen, *Chem. Mater.*, 2011, **23**, 5037–5044.
37 L. Zhao, J. Drennan, C. Kong and S. Amarasinghe, *J. Mater. Chem. A*, 2014, **2**, 11114–11123.
38 F. S. Baumann, J. Fleig, M. Konuma, U. Starke, H.-U. Habermeier and J. Maier, *J. Electrochem. Soc.*, 2005, **152**, A2074–A2079.
39 M. Liu, D. Ding, K. Blinn, X. Li, L. Nie and M. Liu, *Int. J. Hydrogen Energy*, 2012, **37**, 8613–8620.
40 B. Koo, K. Kim, J. K. Kim, H. Kwon, J. W. Han and W. Jung, *Joule*, 2018, **2**, 1476–1499.
41 S. Chen, Y.-Q. Su, P. Deng, R. Qi, J. Zhu, J. Chen, Z. Wang, L. Zhou, X. P. Guo and B. Y. Xia, *ACS Catal.*, 2020, **10**, 4640–4646.
42 H. Zhang and W. Yang, *Chem. Commun.*, 2007, 4215–4217.
43 D. Chen, C. Huang, R. Ran, H. J. Park, C. Kwak and Z. Shao, *Electrochem. Commun.*, 2011, **13**, 197–199.
44 H. Ding, A. V. Virkar, M. Liu and F. Liu, *Phys. Chem. Chem. Phys.*, 2013, **15**, 489–496.
45 J. Druce, H. Tellez, M. Burriel, M. Sharp, L. Fawcett, S. Cook, D. McPhail, T. Ishihara, H. Brongersma and J. Kilner, *Energy Environ. Sci.*, 2014, **7**, 3593–3599.
46 E. J. Crumlin, E. Mutoro, Z. Liu, M. E. Grass, M. D. Biegalski, Y.-L. Lee, D. Morgan, H. M. Christen, H. Bluhm and Y. Shao-Horn, *Energy Environ. Sci.*, 2012, **5**, 6081–6088.
47 E. Mutoro, E. J. Crumlin, M. D. Biegalski, H. M. Christen and Y. Shao-Horn, *Energy Environ. Sci.*, 2011, **4**, 3689–3696.
48 Y.-L. Huang, C. Pellegrinelli, M. Sakbodin and E. D. Wachsman, *ACS Catal.*, 2018, **8**, 1231–1237.
49 J. Hwang, R. R. Rao, Y. Katayama, D. Lee, X. R. Wang, E. Crumlin, T. Venkatesan, H. N. Lee and Y. Shao-Horn, *J. Phys. Chem. C*, 2018, **122**, 20391–20401.
50 J. M. Tascón and L. G. Tejuca, *J. Chem. Soc., Faraday Trans. 1*, 1981, **77**, 591–602.
51 K. Efimov, T. Klande, N. Juditzki and A. Feldhoff, *J. Membr. Sci.*, 2012, **389**, 205–215.
52 A. Yan, M. Cheng, Y. Dong, W. Yang, V. Maragou, S. Song and P. Tsiakaras, *Appl. Catal., B*, 2006, **66**, 64–71.
53 Y. Zhu, J. Sunarso, W. Zhou and Z. Shao, *Appl. Catal., B*, 2015, **172**, 52–57.
54 K. Nomura, Y. Ujihira, T. Hayakawa and K. Takehira, *Appl. Catal., A*, 1996, **137**, 25–36.

 This journal is © The Royal Society of Chemistry 2020